RSC Advances

ROYAL SOCIETY OF CHEMISTRY

www.rsc.org/advances

Effect of type of anions for the synthesis of mesoporous nanostructured MgO, and their excellent adsorption capacity for the removal of toxic heavy metal ions from water

Ipsita Hazra Chowdhury,[a] Arpita Hazra Chowdhury,[a] Pallab Bose,[a] Sanjoy Mandal,[b] and Milan Kanti Naskar[a]*

[a]Sol-Gel Division, [b]Materials Characterization and Instrumentation Division,

CSIR-Central Glass and Ceramic Research Institute, Kolkata 700 032, India

Abstract

Mesoporous MgO nanostructures of different morphologies like nanoplate, nanosheet and nanoparticle assembled microspheres were prepared by a simple hydrothermal method at 180°C/5h in the absence of any organic templates. The products were characterized by X-ray diffraction (XRD), differential thermal analysis (DTA), thermogravimetry (TG), Fourier transform infrared spectroscopy (FTIR), N_2 adsorption-desorption, field emission scanning electron microscopy (FESEM), and transmission electron microscopy (TEM). The role of anions of different magnesium precursors on the morphology, textural properties, and heavy metal ions (Pb(II) and Cd(II)) adsorption capacity of the products was studied. The adsorption data was interpreted with Langmuir and Freundlich models. The effect of contact time, adsorbate concentration, pH and temperature on the adsorption capacity of the products was investigated. Nanosheet-like MgO obtained from chloride and nitrate salts of magnesium having higher pore size rendered better adsorption capacity than that prepared from sulphate and carbonate sources of magnesium. The prepared MgO nanostructures showed maximum adsorption capacities up to 3900 mg/g and 2980 mg/g for Pb(II) and Cd (II) ions, respectively.

*Corresponding author. E-mail: milan@cgcri.res.in, Fax: +91 33 24730957

1. Introduction

Environmental pollution by heavy metal ions, such as Pb(II), Cd(II), Hg(II), As(V) etc. is becoming a serious concern for their toxic effects on human health and living organisms. Therefore, removal of such micro-pollutants from waste water is of great importance. For water purification, the adsorption technique has been extensively used because of its high efficiency, ease of operation and low cost.[1-3] In recent years, water-treatment problems have been resolved by using nanostructured materials as adsorbents because of their high surface area and active adsorption sites. Removal of micro-pollutants i.e., inorganic and organic micro-pollutants from waste water using nanostructured metal oxides have been widely used. However, their synthesis with tunable morphology and textural properties toward the adsorption capacity is still a great challenge.

Hierarchical micro and nanostructured magnesium oxide (MgO) with different level of building components have attracted great interest in recent times because of their unique physical and chemical properties toward excellent adsorption efficiency for the removal of toxic metal ions from waste water. The most conventional method for the synthesis of MgO is thermal decomposition of magnesium hydroxide or carbonate. Many other methods like sol-gel,[4] hydrothermal,[5] chemical gas phase deposition,[6] combustion aerosol synthesis[7] etc. have been reported for the synthesis of MgO. Nanostructured MgO of different shapes has been reported in the literature.[8] Al-Ghamdi *et al.*[9] synthesized MgO nanowires by hydrothermal technique. MgO nanoplates were prepared by chemical precipitation method.[10] T. Selvamani synthesized MgO microsheets by solution-based technique under reflux condition.[11] Recently, we have prepared grainy rod-like porous MgO.[12] Mesoporous MgO has been synthesized by hard templating[13] and soft templating methods.[14,15] Nagappa and Chandrappa[16] prepared mesoporous MgO by

combustion method using glycine as fuel. Necklace-like mesoporous MgO/TiO_2 heterojunction structures were synthesized by Jia *et al*.[17]

In the present study, we have synthesized porous MgO by a simple hydrothermal process using different magnesium salts and urea in the absence of any templating agent. We have shown how the hierarchical 2D and 3D structures of MgO are formed via self-organization of nanoparticles building blocks by simply changing different magnesium salt precursors. Herein, to the best of our knowledge, we report for the first time the role of different anions of the magnesium salt solutions in tuning morphology and surface textural properties toward adsorption efficiency for the removal of Pb(II) and Cd(II) in water.

2. Experimental

2.1 Materials

Magnesium carbonate ($MgCO_3$), magnesium chloride hexahydrate ($MgCl_2.6H_2O$), magnesium nitrate hexahydrate ($Mg(NO_3)_2.\ 6H_2O$), magnesium sulphate heptahydrate ($MgSO_4.\ 7H_2O$), urea, lead nitrate and cadmium nitrate of AR grade each were purchased from Merck, India. Deionized (DI) water was used throughout the experiment.

2.2 Synthesis of MgO nanostructures

In a typical synthesis procedure, 20 mmol urea solution was added into 28 mmol each of $MgCO_3$, $MgCl_2$, $Mg(NO_3)_2$ and $MgSO_4$ solution. The each mix solution was stirred for 30 minutes followed by transferring into 100 mL Teflon-lined autoclave. The autoclave was kept in an oven at 180^{o}C for 5 hours. After the reaction, the particles were collected by centrifugation and washing with DI water, and dried at 60^{o}C for 4 h. The dried as-prepared samples were calcined at 600^{o}C for 2 hours. The as-prepared samples were designated as MAP-C, MAP-Cl, MAP-N and MAP-S obtained from $MgCO_3$, $MgCl_2$, $Mg(NO_3)_2$ and $MgSO_4$, respectively, while

the corresponding oxide samples after calcinations at 600°C were marked as MgO-C, MgO-Cl, MgO-N and MgO-S, respectively.

2.3 Characterization

X-ray diffraction (XRD) studies of the sample was performed by Philips X'Pert Pro PW 3050/60 powder diffractometer using Ni-filtered Cu-K_α radiation (λ = 0.15418 nm) operated at 40 kV and 30 mA. The crystallite size (d) of MgO was determined by XRD peak analysis based on Scherrer's equation: $d = 0.9\lambda/B\cos\theta$, where, λ is the wavelength of Cu-K_α, B is the full width at half maximum (FWHM) of the intensity peak in radian, and θ is the angle of the largest peak. The thermal behavior of the sample was studied by differential thermal analysis (DTA) and thermogravimetry (TG) (Netzsch STA 449C, Germany) from 30° to 1000°C in air atmosphere at the heating rate of 10°C min^{-1}. The characteristic vibration bands of the product were confirmed by Fourier transform infrared (FTIR; Nicolet 5PC, Nicolet Analytical Instruments, Madison, WI) with KBr pellet at a resolution of 4 cm^{-1}. Nitrogen adsorption and desorption measurements were performed at liquid nitrogen temperature (77 K) on a Quantachrome (ASIQ MP) instrument. The sample was outgassed in vacuum at 200 °C for 4 h prior to measurement. The total surface area was determined by Brunauer-Emmett-Teller (BET) method within the relative pressure (*p/po*) range of 0.05-0.20, and the pore size distributions were calculated by the Barrett-Joyner-Halenda (BJH) method. The total pore volume was estimated from the amount of nitrogen adsorbed at the relative pressure (*p/po*) of ca 0.99. The morphology of the particles was examined by FESEM (Model: Zeiss, Supra™ 35VP, Oberkochen, Germany) operating with an accelerating voltage of 10 kV, and transmission electron microscopy (TEM), using a Tecnai G2 30ST (FEI) instrument operating at 300 kV.

2.4 Heavy metal ions adsorption test

Aqueous solutions with different concentrations of Pb (II) and Cd(II) ions were prepared using lead nitrate and cadmium nitrate as the sources of heavy metal ions. The pH of the each solution was adjusted to 7. For the adsorption kinetic study, 10 mg of MgO particles obtained from different sources were added into 15 mL each of Pb (II) and Cd(II) solutions with an initial concentration of 100 mg/L each. After a specified time, the solid and liquid were separated immediately and the supernatants were analyzed by inductively coupled plasma−atomic emission spectroscopy (ICP-AES) (Model: Spectro Ciros Vision, Germany) to measure the concentration of metal ions after adsorption. For the adsorption isotherm study, 10 mg of adsorbent was added into 15 mL solution with different concentrations of Pb (II) and Cd(II) under stirring at room temperature **(35^{o}C)** for 2 h. The adsorption data was fitted with the Langmuir model as follows:

$$q_e = q_m b C_e / (1 + \mathbf{K_L}\, C_e) \qquad (1)$$

Where, C_e = equilibrium concentration of heavy metal ions (mg/L),

q_e = amount of heavy metal ions adsorbed per unit weight of the adsorbent at equilibrium (mg/g),

q_m = maximum adsorption capacity (mg/g) and

K_L= adsorption constant (L/mg) related to the energy of adsorption.

The linear form of the Langmuir isotherm is represented by the following equation:

$$C_e/q_e = C_e/q_m + 1/K_L.q_m \qquad (2)$$

A plot of C_e/q_e vs C_e will give a straight line with slope $1/q_m$, and intercept $1/K_L.q_m$.

The Freundlich isotherm describes heterogeneous surface with a non-uniform distribution of heat of adsorption over the surface. The linear form of Freundlich isotherm is expressed as:

$$\log q_e = \log K_F + 1/n_F \log C_e \qquad (3)$$

Where, K_F is the Freundlich constant (L/mg) indicating adsorption capacity and n_F is the heterogeneity factor. Values $n_F > 1$ represent favorable adsorption conditions. In most cases, the exponent between $1 < n_F < 10$ shows beneficial adsorption. A plot of log q_e vs log C_e will give a straight line with slope $1/n_F$, and intercept log K_F.

3. Results and Discussion:

3.1 Characterization of MgO nanostructure

Fig. 1a shows the XRD pattern of as-prepared samples: (i) MAP-C, (ii) MAP-Cl, (iii) MAP-N and (iv) MAP-S. Monoclinic hydromagnesite phase ($Mg_5(CO_3)_4(OH)_2.4H_2O$ (JCPDS 25-513) was obtained from MAP-C, MAP-Cl and MAP-N, while MAP-S rendered cubic magnesium oxide carbonate ($Mg_3O(CO_3)_2$) as major phase (JCPDS 31-804) containing a little amount of hydromagnesite phase. After calcinations of the samples at 600 ^oC, the as-prepared samples prepared from different sources of magnesium were completely converted to cubic MgO (JCPDS 45-946) indicating the crystal planes at (111), (200), (220), (311) and (222) (Fig. 1b).

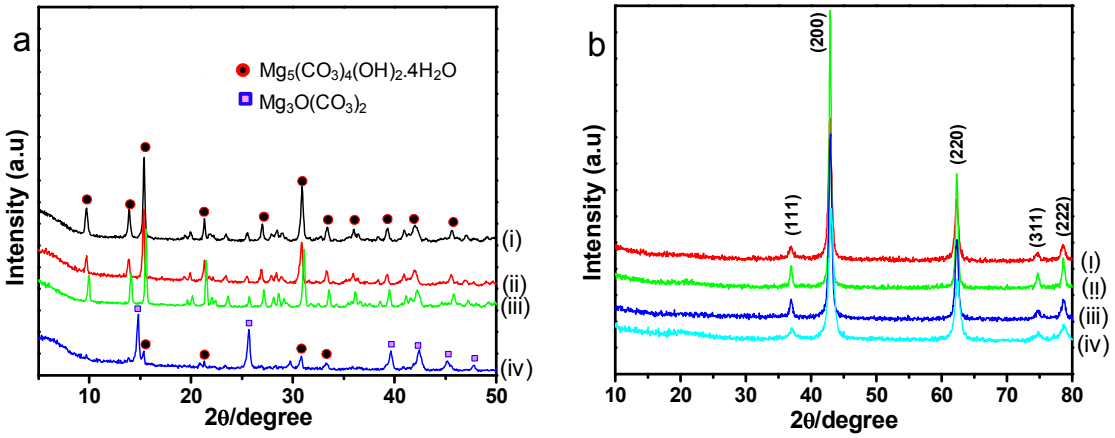

Fig. 1: XRD patterns of (a) as-prepared samples: (i) MAP-C, (ii) MAP-Cl, (iii) MAP-N and (iv) MAP-S, and (b) calcined (600^oC) samples: (i) MgO-C, (ii) MgO-Cl, (iii) MgO-N and (iv) MgO-S.

Figure 2 shows the TG and DTA curves of the as-prepared samples: (a) MAP-C, (b) MAP-Cl, (c) MAP-N and (d) MAP-S. In TG analysis, it is observed that mass loss of about 52-

56% occurred for all the samples. The mass loss was attributed to the removal of surface adsorbed water, crystalline water, and dehydroxylation and decarboxylation of the compound $Mg_5(CO_3)_4(OH)_2.4H_2O$. Practically, no mass loss was observed above 600 ^oC. In the DTA analysis, two distinct endothermic peaks at around 265-300^o and 430-455 ^oC were observed for the samples MAP-C, MAP-Cl and MAP-N, while the sample MAP-S exhibited the endothermic peaks at 385 ^{o}, 470 ^{o}, 505 ^{o} and 545 ^oC. The endothermic peaks corroborated to the dehydration of crystalline water as well as dehydroxylation and decarboxylation of the compound $Mg_5(CO_3)_4(OH)_2.4H_2O$.[11,12,18,19] The appearance of exothermic peaks at around 485-520 ^oC could be assigned to the crystallization of $MgCO_3$.[20] From thermal analysis, the probable decomposition reaction could be summarized as follows:

$$Mg_5(CO_3)_4(OH)_2.4H_2O \rightarrow Mg_5(CO_3)_4(OH)_2 + 4H_2O \quad (1)$$

$$Mg_5(CO_3)_4(OH)_2 \rightarrow 4MgCO_3 + MgO + H_2O \quad (2)$$

$$MgCO_3 \rightarrow MgO + CO_2 \quad (3)$$

$$Mg_3O(CO_3)_2 \rightarrow 3MgO + 2CO_2 \quad (4)$$

For the precursors, $MgCO_3$, $MgCl_2$ and $Mg(NO_3)_2$, the reactions (1) to (3) occurred, while $MgSO_4$ facilitated to proceed the reactions (1) to (4).

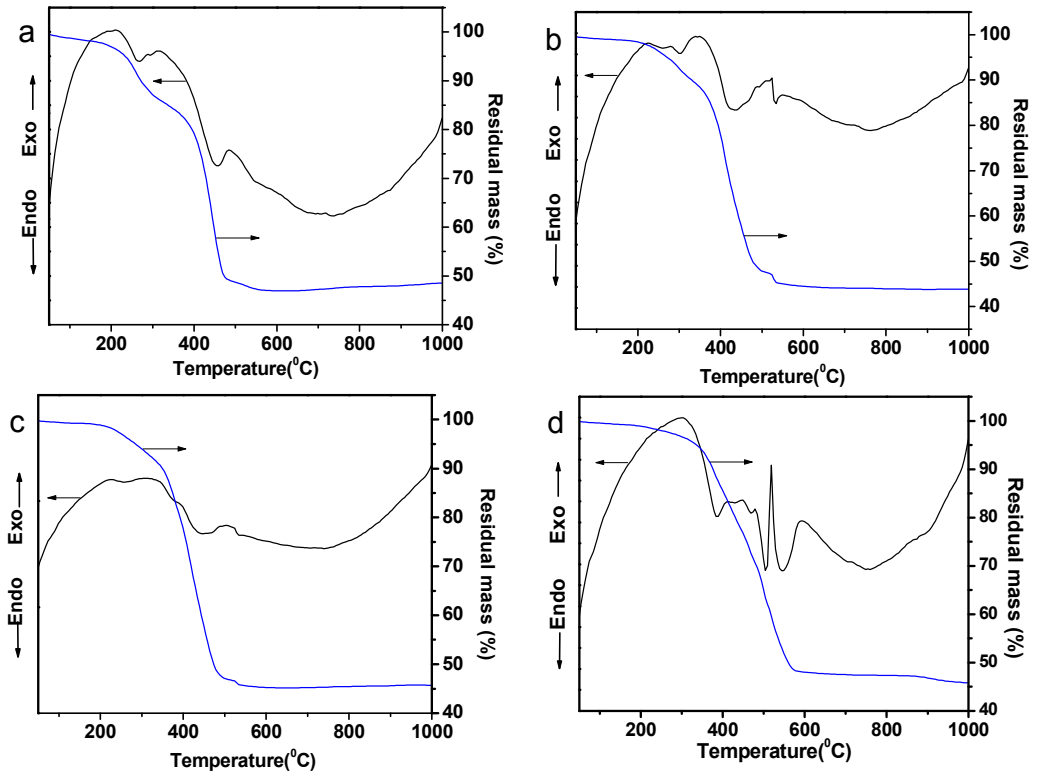

Fig. 2: TG and DTA curves of the as-prepared sample: (a) MAP-C, (b) MAP-Cl, (c) MAP-N and (d) MAP-S.

Figure 3 shows the FTIR spectra of (a) as-prepared and (b) 600°C-treated sample. In the as-prepared samples, the intense peak at around 3650 and 3450 cm^{-1} were due to the structural and adsorbed OH groups, respectively. The symmetric and asymmetric stretching vibrations of carbonate (CO_3^{2-}) ions were noticed at about 1120 and 1475-1422 cm^{-1}, respectively, while the corresponding bending vibration bands were observed at about 850 and 885 cm^{-1}.[21] The absorption bands at 1120 and 1034 cm^{-1} were also the characteristic asymmetric and symmetric stretching vibrations of SO_4^{2-} ions (MAP-S), respectively.[22] For the oxide samples after calcinations at 600 °C, the characteristic Mg-O stretching vibration was confirmed at around 435, 585 and 860 cm^{-1}.[23] In the oxide samples, the broad vibration bands at around 1440 cm^{-1} indicated that some CO_3^{2-} ions could be entrapped into the porous oxide samples. It is clear that

CO_2 and H_2O molecules forming CO_3^{2-} ions in exposed atmospheres were chemisorbed as a monodentate fashion onto MgO.[24] The presence of small absorption band at around 1120 cm^{-1} could ascertain that a little fraction of SO_4^{2-} ions could be present in the sample, MgO-S.

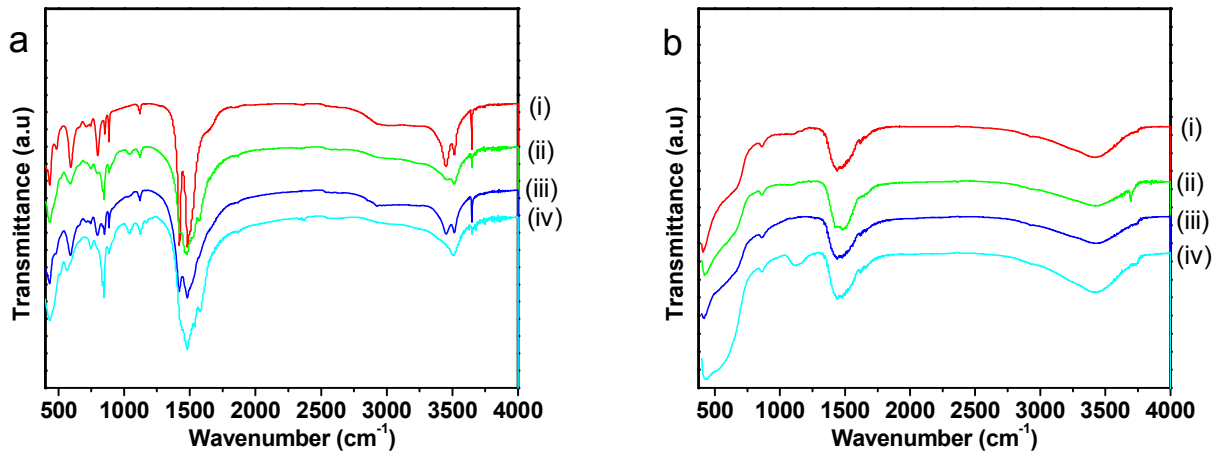

Fig. 3: FTIR spectra of (a) as-prepared samples: (i) MAP-C, (ii) MAP-Cl, (iii) MAP-N and (iv) MAP-S, and (b) calcined (600^oC) samples: (i) MgO-C, (ii) MgO-Cl, (iii) MgO-N and (iv) MgO-S.

Figure 4 shows the N_2 adsorption-desorption isotherms of MgO samples. It indicates type III isotherm with H3 hysteresis loop. The appearance of this type of hysteresis is due to slit-like pores with nonuniform size and/or shape.[25] It is to be noted that uptake of nitrogen increased steeply above the relative pressures (*p/po*) of about 0.70, 0.85 and 0.90 for the samples MgO-S and MgO-N, MgO-Cl and MgO-C, respectively. It could reflect their surface area and pore geometry. The corresponding BJH pore size distributions (PSDs) derived from desorption data of the isotherms are shown in the insets of Fig. 4. The nature of the PSDs curves also confirms the absence of regular shape and size of the pores in the samples. A wider PSD was noticed in the samples, MgO-Cl and MgO-N, respectively, while MgO-C and MgO-S rendered narrower PSDs with smaller pores.

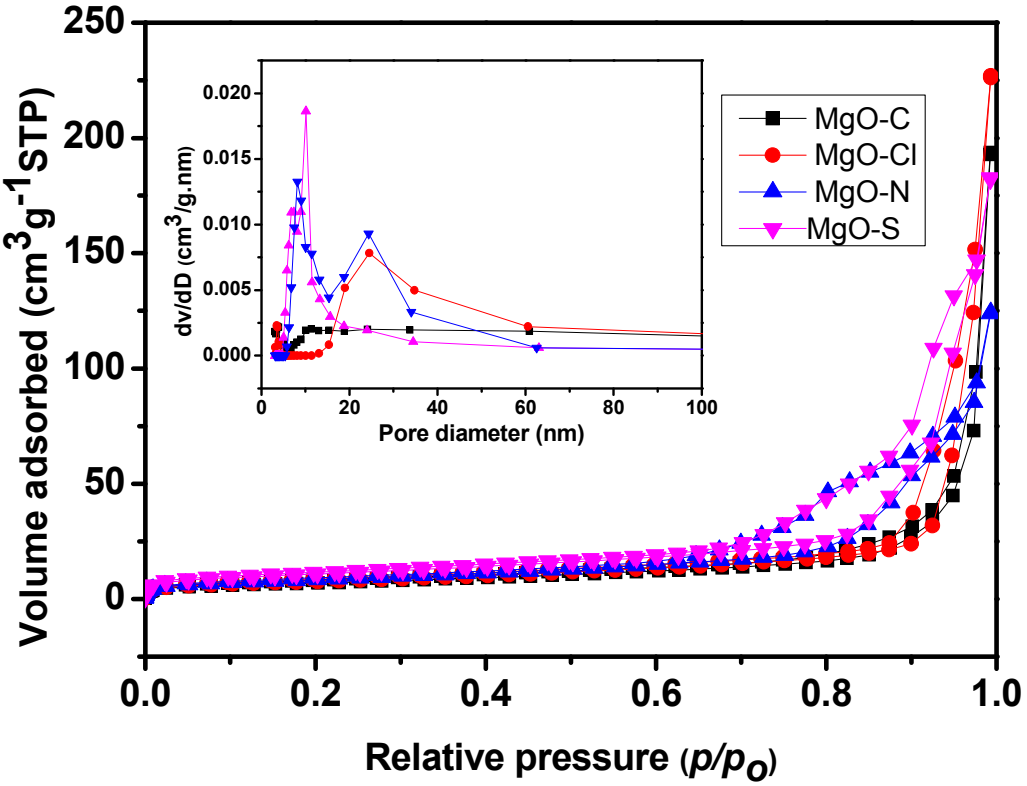

Fig. 4: N_2 adsorption-desorption isotherms of the samples: (i) MgO-C, (ii) MgO-Cl, (iii) MgO-N and (iv) MgO-S. Insets show the corresponding pore size distributions.

The textural properties (BET surface area, total pore volume and pore size) and crystallite size of all the samples are summarized in Table 1. For different sample, the BET surface area increased in the order of MgO-C<MgO-Cl<MgO-N<MgO-S. Unlike the sample MgO-C, the increase in surface area values in the order of MgO-Cl<MgO-N<MgO-S could be explained based on their decrease in pore size and crystallite size.[26] The pore diameter increased with increase in crystallite size of the samples (Table 1). However, for the sample MgO-C, the surface area was lower instead of smaller pore size. In addition to pore size, the pore geometry could have

significant effect on the surface area,[25] which was revealed by the sample, MgO-C. The sample, MgO-Cl exhibited larger pore size with maximum pore volume followed by MgO-N, MgO-S and MgO-C, respectively. It is interesting to note that the crystallite size of MgO-Cl was bigger than that of other samples (Table 1), which could be due to higher solid state diffusion of the particles in MgO-Cl sample during calcination. This bigger crystallite size causes larger interparticle porosity in MgO-Cl compared to other samples.

Table 1. Textural properties and crystallite size of the samples calcined at 600^{o}C

Sample ID	S_{BET} (m^2g^{-1})[a]	$V_{p\text{-}Total}$ (cm^3g^{-1})[b]	D_{BJH} (nm)[c]	Crystallite size (nm)
MgO-C	24.9	0.30	3.7	27.6
MgO-Cl	27.5	0.35	24.5	49.6
MgO-N	30.4	0.19	10.1	29.8
MgO-S	38.8	0.28	8.2	19.4

[a]BET surface area; [b]Total pore volume; [c]pore diameter by BJH adsorption.

Figure 5 shows the FESEM images of the as-prepared samples: (a) MAP-C, (b) MAP-Cl, (c) MAP-N and (d) MAP-S. It is noticed that the as-prepared hydromagnesite obtained from $MgCl_2$ and $Mg(NO_3)_2$ precursors were nanoflake-like morphology, while that obtained from $MgCO_3$ rendered nanoplate-like architecture. However, as-prepared magnesium oxide carbonate ($Mg_3O(CO_3)_2$) obtained from $MgSO_4$ revealed spherical morphology comprising of self-assembled nanoparticles. Some hollow microspheres were also obtained from $MgSO_4$ precursor. Figure 6 shows the FESEM images of the calcined (600^{0}C) samples: (a, b) MgO-C, (c, d) MgO-Cl, (e, f) MgO-N and (g, h) MgO-S. It is interesting to note that the nanoplate-like microstructure

obtained from $MgCO_3$ (Fig. 6a,b), and spherical morphology obtained from $MgSO_4$ remained intact after calcination. However, the nanoflake-like morphology obtained from $MgCl_2$ and $Mg(NO_3)_2$ changed to nanosheet-like structure after heat-treatment. In the nanosheet-like particles, the smaller nanoparticles were arranged in a linear alignment forming a chain-like structure (Fig. 6d,f). The morphology of the corresponding samples was shown in TEM images (Fig. 7). The interparticle porosity in the samples was clearly revealed in the TEM images. Figure 8 shows the HR-TEM images of the samples, (a) MgO-C, (b) MgO-Cl, (c) MgO-N and (d) MgO-S. The d-spacing of 0.21 nm was attributed to the (200) lattice planes of cubic MgO. The selected area electron diffraction (SAED) patterns of the corresponding samples (shown in the insets) indicated the polycrystalline nature of MgO. The bright spots of the concentric rings matched well with the MgO planes obtained from XRD.

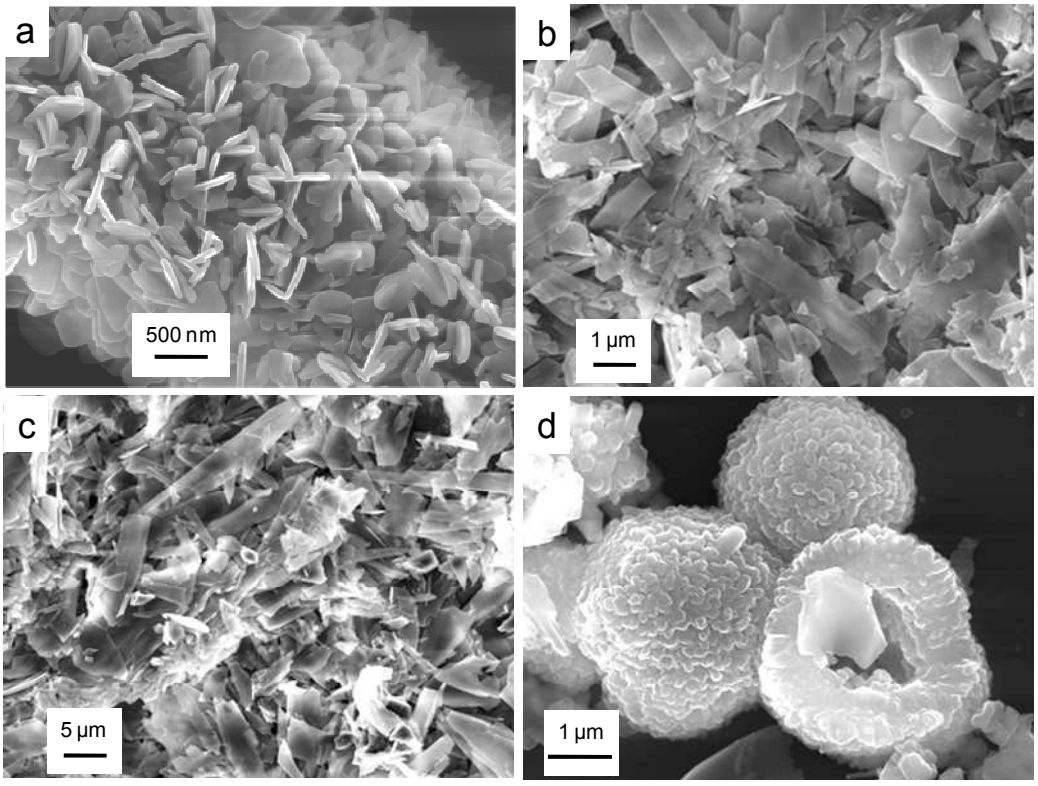

Fig. 5: FESEM images of the as-prepared samples: (a) MAP-C, (b) MAP-Cl, (c) MAP-N and (d) MAP-S.

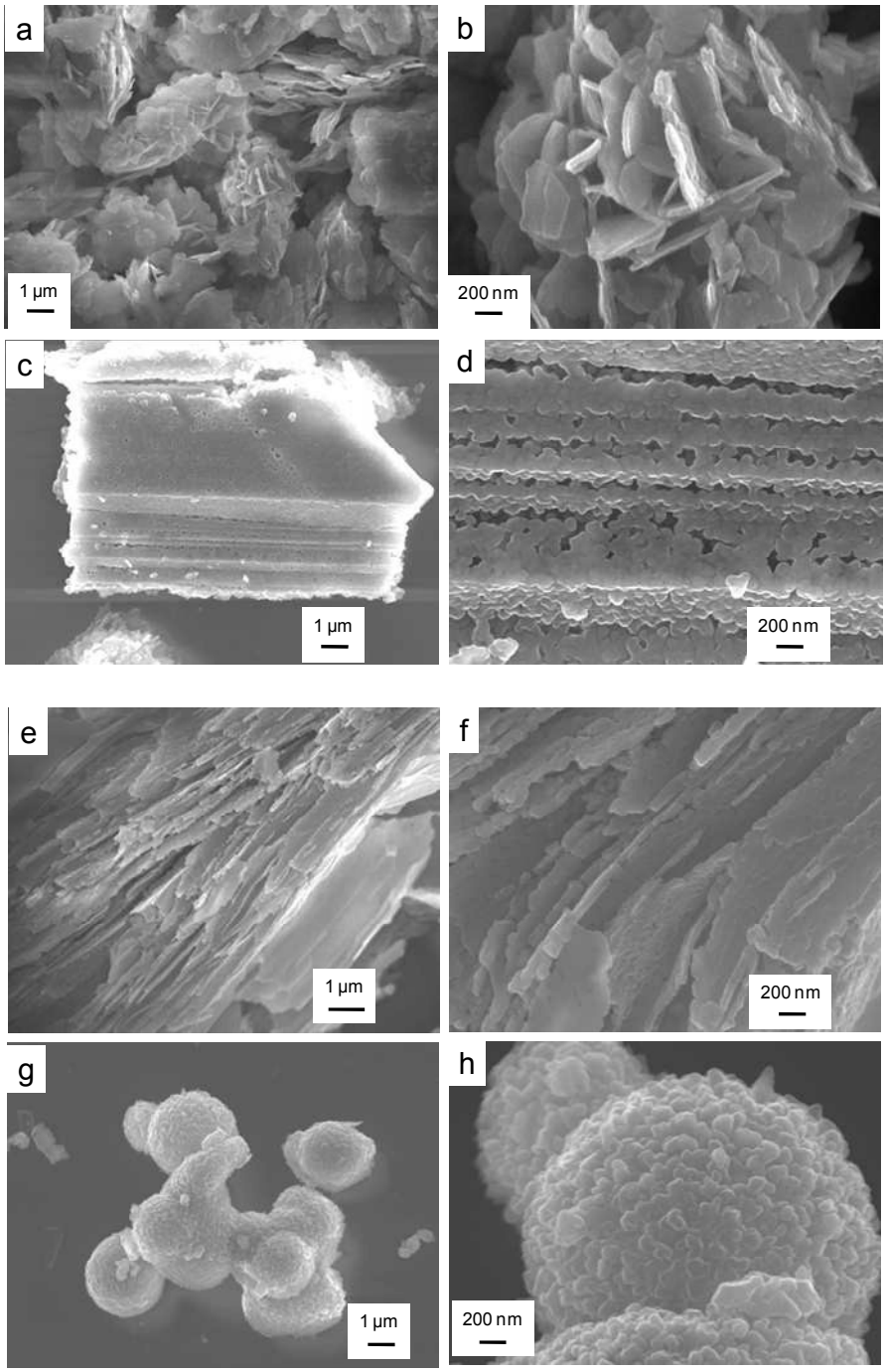

Fig. 6: FESEM images of the calcined (600°C) samples: (a,b) MgO-C, (c,d) MgO-Cl, (e,f) MgO-N and (g,h) MgO-S.

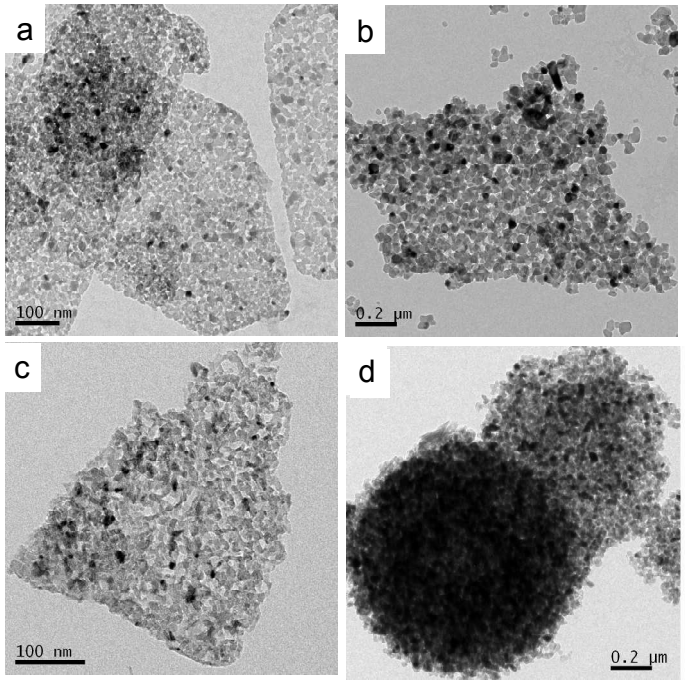

Fig. 7 TEM images of the calcined (600°C) samples: (a) MgO-C, (b) MgO-Cl, (c) MgO-N and (d) MgO-S.

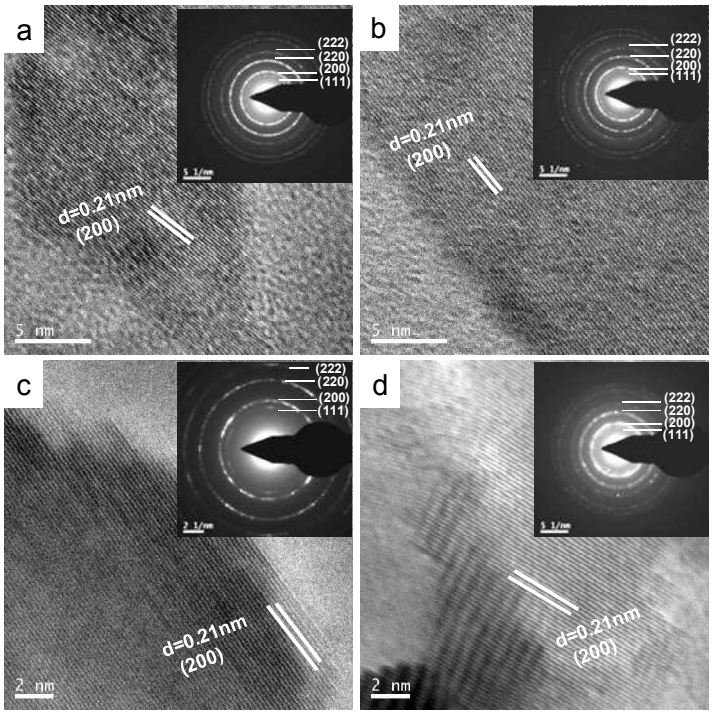

Fig. 8: HRTEM images of the calcined (600°C) samples: (a) MgO-C, (b) MgO-Cl, (c) MgO-N and (d) MgO-S. Insets show the corresponding SAED patterns.

A probable reaction mechanism can be illustrated for the formation of as-prepared nanoarchitectured products. Under hydrothermal condition at 180°C/5h, urea decomposes slowly with the formation of NH_3 and CO_2 followed by their hydrolysis producing OH^- and HCO_3^- ions. In the reaction medium, different magnesium salts interact with the anions (OH^- and HCO_3^-) forming the nuclei of hydromagnesite ($Mg_5(CO_3)_4(OH)_2.4H_2O$) and/or magnesium oxide carbonate ($Mg_3O(CO_3)_2$). The respective reactions in the presence of different anions of Mg^{2+} are expressed as follows:

$$CO(NH_2)_2 + H_2O \rightarrow 2\ NH_3 + CO_2 \quad (5)$$

$$NH_3 + H_2O \rightarrow NH_4^+ + OH^- \quad (6)$$

$$CO_2 + H_2O \rightarrow H^+ + HCO_3^- \quad (7)$$

$$5MgCO_3 + 6OH^- + 4HCO_3^- \rightarrow Mg_5(CO_3)_4(OH)_2.4H_2O + 5\ CO_3^{2-} \quad (8)$$

$$5MgCl_2 + 6OH^- + 4HCO_3^- \rightarrow Mg_5(CO_3)_4(OH)_2.4H_2O + 10\ Cl^- \quad (9)$$

$$5Mg(NO_3)_2 + 6OH^- + 4HCO_3^- \rightarrow Mg_5(CO_3)_4(OH)_2.4H_2O + 10\ NO_3^- \quad (10)$$

$$8MgSO_4 + 10OH^- + 6HCO_3^- \rightarrow Mg_3O(CO_3)_2 + Mg_5(CO_3)_4(OH)_2.4H_2O + 8\ SO_4^{2-} + 3H_2O \quad (11)$$

Scheme 1 shows the probable growth process of the as-prepared products. The free anions (CO_3^{2-}, Cl^-, NO_3^-, SO_4^{2-}) are produced during the chemical reactions shown above (8-11). These anions along with OH^- and HCO_3^- ions adsorbed preferably on the well-aligned as-prepared hydroxide surfaces either through hydrogen bonding or through loose coordination with Mg^{2+}. As the reaction proceeds, OH^- and HCO_3^- ions are adsorbed in an alternative way onto the major crystallographic plane of the hydromagnesite nuclei forming plate and flake-like 2D nanostructures in the presence of $MgCO_3$, and $MgCl_2/Mg(NO_3)_2$, respectively. Interestingly, in

the presence of $MgSO_4$, the growth of the particles occurred in all possible direction forming 3D microsphere of magnesium oxide carbonate ($Mg_3O(CO_3)_2$). The 3D self-assembly of magnesium oxide carbonate particles occurred through the bridging of SO_4^{2-} ions via hydrogen bonding with the surface adsorbed hydroxyl ions resulting spherical microstructure with hollow cavity in the interior. It is to be noted that the presence of SO_4^{2-} ions were confirmed by FTIR study. The interior cavity was gradually formed via a core evacuation process, through a mechanism similar to Ostwald ripening.[27] During thermal decomposition, dehydroxylation and decarboxylation occurred in $Mg_5(CO_3)_4(OH)_2.4H_2O$ and $Mg_3O(CO_3)_2$ with the release of H_2O, CO_2 and other volatiles like entrapped NH_3, Cl_2, NO_2, SO_2 etc. It causes interparticle porosity forming porous MgO.

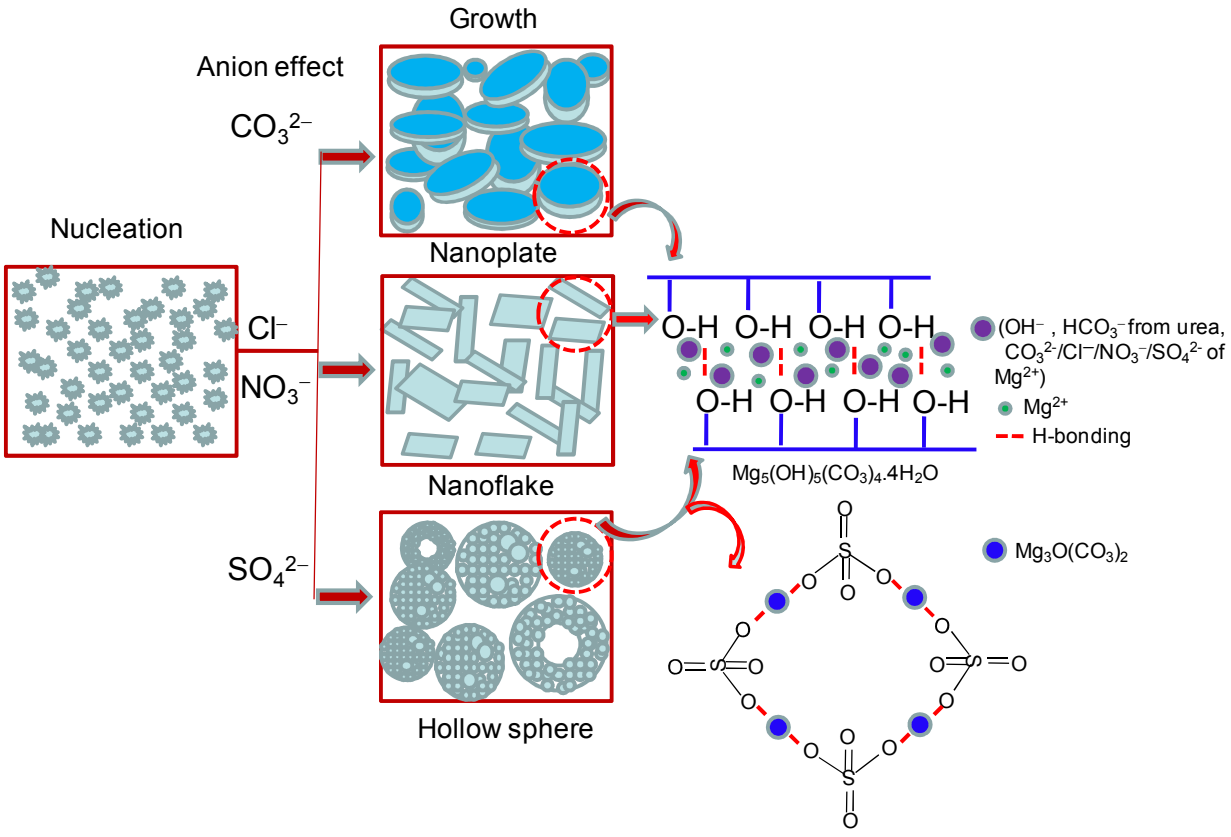

Scheme 1: Schematic illustration for the formation of as-prepared nanostructures

3.2 Heavy metal ion adsorption study

Heavy metal cations like Pb(II) and Cd(II) are toxic in drinking water resources. It is critical issue for their efficient removal from drinking water. The adsorption efficiency of MgO nanostructures as adsorbents for the removal of Pb(II) and Cd(II) ions was performed by varying contact time, adsorbate concentration, pH and temperature. Fig. S1 (ESI) shows the adsorption of Pb(II) ions (initial concentration of 100 mg/L at pH 7) with contact time at 35^{o}C for the samples: (a) MgO-C, (b) MgO-Cl, (c) MgO-N and (d) MgO-S, while the adsorption of Cd(II) ions with contact time for the above samples with the same experimental parameters is depicted in Fig. S2 (ESI). It is noticed that the adsorption processes for Cd(II) ions with all the samples were becoming very fast rendering no significant difference in the adsorption efficiency for different samples. Within 5 min, all the MgO samples adsorbed around 99% of Pb(II) ions and 100% of Cd(II) ions. The initial rapid adsorption rate is due to the availability of abundant active sites on the surface of MgO samples. The kinetics of Pb(II) and Cd(II) removal were investigated. The data were fitted well to a pseudo-second-order[28] model (k_2, g mg^{-1} min^{-1}) as shown in the insets of Fig. S1 and S2 for the adsorption of Pb(II) and Cd(II) ions, respectively. The k_2 values and the amounts of heavy metal ions adsorbed at equilibrium (q_e, mg g^{-1}) were calculated from the slope and intercept of the plots of t/q_t versus t according to the equation.[29]

$$t/q_t = 1/k_2 q_e^2 + t/q_e \qquad (4)$$

where q_t is the amount of adsorbed ion (mg g^{-1}) at time t. Table S1 shows the calculated q_e, k_2, and regression coefficient (R^2) values. The R^2 values are close to unity indicating best fit with pseudo-second-order model. In this model, the rate determining step is the surface adsorption involving chemisorption process.

The adsorption data at pH 7obtained from ICP analysis showed the highest maximum adsorption capacity for Pb(II) and Cd(II) as reported in the literature[30-34] (Table 2).

Table 2. Adsorption capacity of the samples for Pb (II) and Cd(II) ions at pH 7

Sample ID	Adsorption capacity (mg/g)	
	Pb(II)	Cd(II)
MgO-C	2550	2491
MgO-Cl	3450	2938
MgO-N	3900	2980
MgO-S	3150	2629

The adsorption of Pb(II) and Cd(II) ions with their different dosages on MgO samples was studied at pH 7 with contact time of 2 h at 35°C. Figure 9 shows the adsorption isotherms (derived from equation 1) obtained with different initial concentrations ranging from 100 to 5000 mg/L of (a) Pb(II) and (b) Cd(II) ion. It is mentioned worthy that the adsorption capacity of MgO obtained from different sources followed as: MgO-N > MgO-Cl > MgO-S > MgO-C.

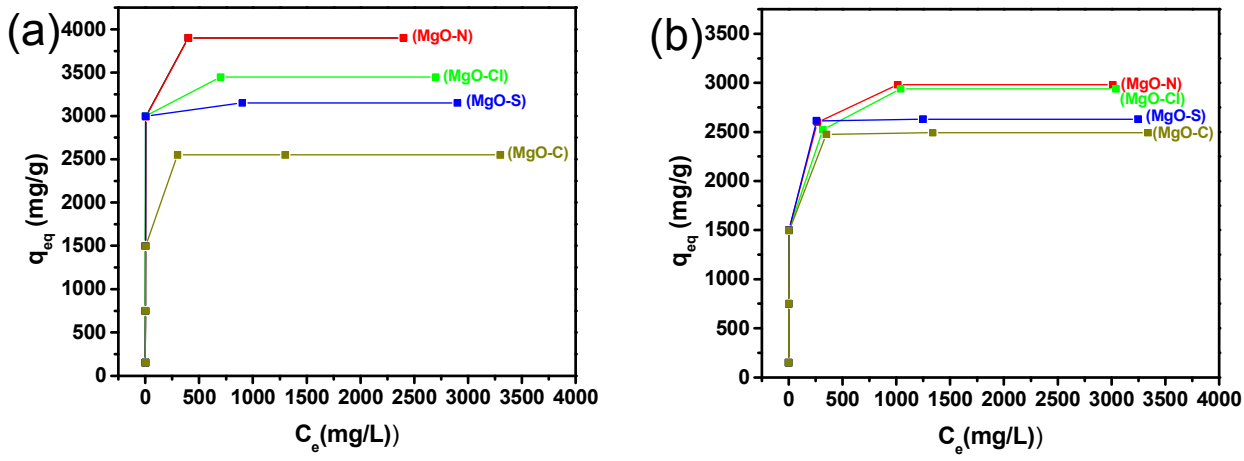

Fig. 9: Adsorption isotherms obtained with different initial concentrations of (a) Pb(II) and (b) Cd(II) ions for the samples: (i) MgO-C, (ii) MgO-Cl, (iii) MgO-N and (iv) MgO-S.

The pH of aqueous solution is an important factor to influence the adsorption efficiency of metal ions.[35] Thus, the adsorption of Pb(II) and Cd(II) ions on the surface of MgO samples was investigated with different pH ranging from 3.0 to 7.0 keeping the initial metal ion concentration of 5000 ppm, contact time of 2 h and temperature at 35°C (Fig. 10). It is interesting that the amount of Pb(II) and Cd(II) ions adsorption on MgO samples increased with increasing pH. It is to be noted that at lower pH, the overall surface charge on the active sites became positive. The metal ions and protons could compete for binding sites on the surface walls of adsorbent (MgO samples), resulting in lower uptake of metal ions.[36] However, at higher pH having less number of protons, the adsorption of metal ions are enhanced. Interestingly at each pH, the adsorption efficiency of MgO followed the order as: MgO-N > MgO-Cl > MgO-S > MgO-C.

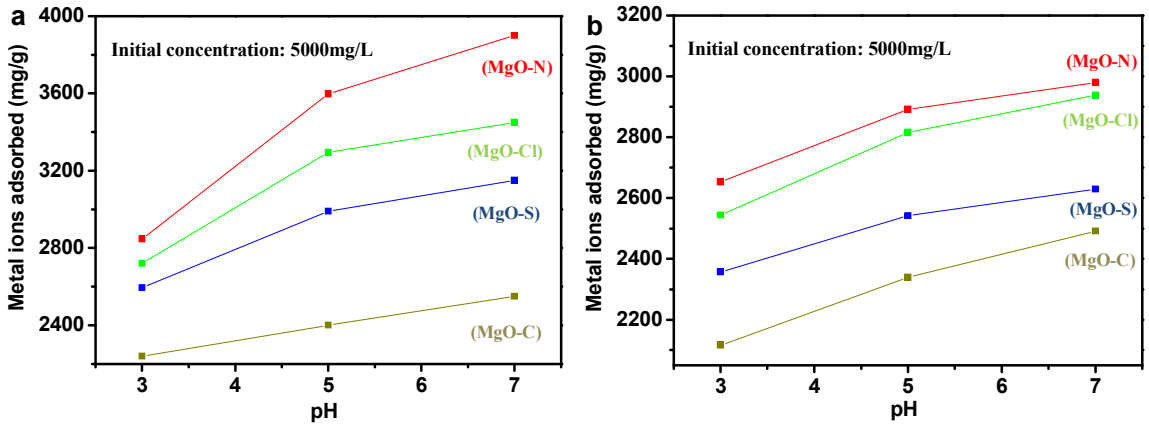

Fig. 10: Effect of pH for the adsorption of (a) Pb(II) and (b) Cd(II) ions on MgO samples

The adsorption of Pb(II) and Cd(II) ions on MgO samples was studied with different temperatures keeping the initial metal ion concentration of 5000 ppm at pH 7 and contact time of 2 h (Fig. 11). It is clear that with increase in temperatures the adsorption of heavy metal ions increased. This could be due to higher kinetic energy acquired by the metal ions with increase in temperature resulting in their facile adsorption on MgO samples.

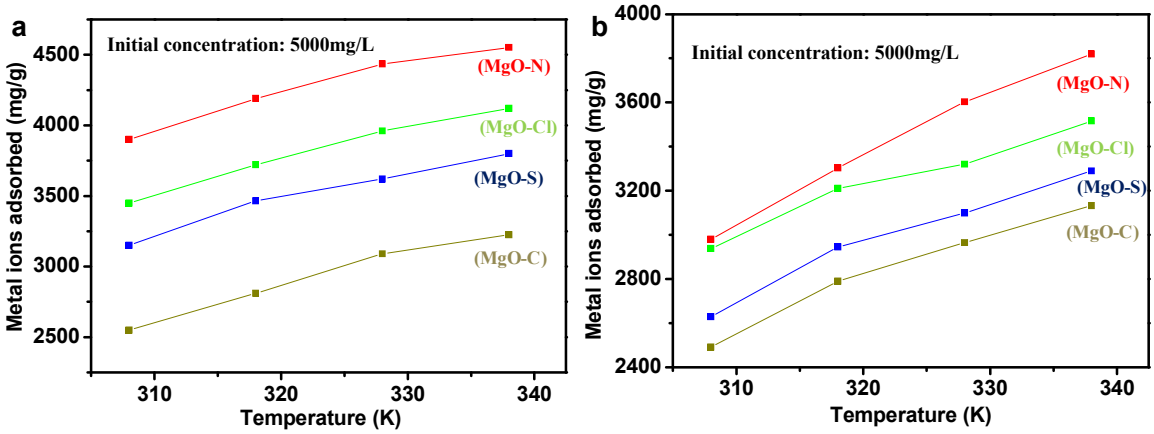

Fig. 11: Effect of temperature for the adsorption of (a) Pb(II) and (b) Cd(II) ions on MgO samples.

An adsorption isotherm describes the relationship between the amount of adsorbate that is adsorbed on the adsorbent and the concentration of dissolved adsorbate in the liquid medium at equilibrium. The experimental data of adsorption isotherms has been fitted with Langmuir and Freundlich models. The Langmuir isotherm assumes monolayer coverage of adsorbate onto a homogeneous adsorbent surface, whereas the Freundlich isotherm is suitable for a highly heterogeneous surface. The linear plots of Langmuir isotherms (equation 2) for the removal of Pb(II) and Cd(II) are shown in Figs. S3 and S4, respectively for the samples (a) MgO-C, (b) MgO-Cl, (c) MgO-N and (d) MgO-S each, while the Freundlich isotherms (equation 3) of the corresponding samples are depicted in Figs. S5 and S6, respectively. The parameters obtained from the different models are listed in Table 3. The linear regression coefficient (R^2) values based on the actual deviation between the experimental and theoretical data render a better correlation of experimental data. From the isotherm data (Table 3) it is clear that Langmuir isotherm model is well fitted for the adsorption of Pb(II) and Cd(II) ions. However, for Freundlich isotherms, the values of n_F (heterogeneity factor) are in the range of 1 to 10 which

represents favorable adsorption.[37] The Gibbs free energy change, ΔG^o for the adsorption process indicates the degree of spontaneity of the adsorption. It is represented by the following equation:

$$\Delta G^o = -RT \ln K \quad (5)$$

Where, K is the thermodynamic equilibrium constant, R is the universal gas constant (8.314 J/mol/K) and T is temperature (K). The values of K can be determined by plotting ln (q_e/C_e) against q_e and extrapolating to zero (q_e is the adsorbed heavy metals ion concentration at equilibrium and C_e is the equilibrium concentration of heavy metals ion in solution).[38] The ΔG^o values for the adsorption process at 35°C (308K) are summarized in Table 3. The negative values of $\Delta G°$ indicate the spontaneous adsorption of Pb(II) and Cd(II) ions.

Table 3: The parameters obtained from Langmuir and Freundlich models, and Gibbs free energy change.

Heavy metal ions		Pb (II)				Cd (II)			
Sample ID		MgO-C	MgO -Cl	MgO -N	MgO -S	MgO-C	MgO -Cl	MgO -N	MgO -S
Langmuir	q_m(mg/g)	2550	3450	3900	3150	2491	2938	2980	2629
	K_L (L/mg)	0.765	0.966	0.786	0.359	0.948	0.089	0.076	0.986
	R^2	0.999	0.999	0. 999	0.998	0.999	0.998	0.999	0.999
Freundlich	K_F (mg/g)	912.01	891.2	1023.2	912.01	933.2	954.9	977.2	933.2
	n_F	7.14	5.00	5.34	5.58	7.57	6.62	6.53	6.80
	R^2	0.941	0.925	0.873	0.926	0.917	0.922	0.924	0.904
ΔG^O at 35°C (KJ/mol)		-25.35	-20.48	-21.51	-21.76	-29.96	-27.39	-21.17	-27.14

From the above results it is clear that for the removal of heavy metal ions, the adsorption capacity of MgO obtained from different sources followed as: MgO-N > MgO-Cl > MgO-S > MgO-C. It can be explained by the textural property and morphology of the respective samples. The BET surface area for different samples were in the order of MgO-S > MgO-N > MgO-Cl > MgO-C. With the exception for the sample MgO-S, the adsorption capacity increased with increase in surface area. Instead of maximum surface area of the sample MgO-S, its adsorption capacity was not significantly increased. It could be due to smaller pore size and spherical morphology of the sample. It is worth noting that adsorption efficiency is related not only with the surface area but morphology plays a significant role. In the present study nanosheet structures of MgO-N and MgO-Cl possess more active sites than spherical MgO-S samples toward favorable adsorption efficiency.

In the adsorption process, after each adsorption, the concentrations of Mg^{2+} in solution were tested. It was observed that with increase in adsorption of heavy metal ions (Pb(II), Cd(II)), the concentration of Mg^{2+} ions in solution increased (Fig. **S7**, ESI). It indicated that cation exchange mechanism took place between Mg^{2+} and Pb(II) or Cd(II) which was confirmed by the XRD study of MgO after adsorption of Pb(II) (**S8**, ESI). It revealed the characteristic peaks of $Pb_5O_3(OH)_4$ (JCPDS No. 28-536), MgO (JCPDS No. 45-946) and $Mg(OH)_2$ (JCPDS No.7-239). The peaks of $Mg(OH)_2$ could be due to hydrolysis of MgO in water. It suggested that MgO interacted with Pb^{2+} in solution forming $Pb_5O_3(OH)_4$ and $Mg(OH)_2$. The tentative solid-liquid interfacial reaction is proposed as:

$$5Pb^{2+} + 3MgO + 6H_2O = 3Mg^{2+} + Pb_5O_3(OH)_4 + 8H^+ \quad (12)$$

It is worth mentioning that Mg^{2+} ions could remain in the treated drinking water. However, its concentration is still far below the WHO limit for Mg (450mg/L). Thus, MgO nanostructures could be used as safe adsorbents for the removal of Pb(II)and Cd(II) ions from water.

4. Conclusions

In summary, MgO nanostructures of different morphologies (nanoplate, nanosheet and microspheres) were successefully synthesized via a simple template-free hydrothermal method. The influence of anions in different magnesium sources on the structure and textural properties of the products was studied. The pore size, pore geometry, crystallite size and morphology of MgO nanostructures influenced the surface area of the products. The adsorption of Pb(II) and Cd(II) ions onto the MgO samples was affected by their surface area and morphology. The nanosheet structures of MgO-N and MgO-Cl possess more active sites than spherical MgO-S samples toward favorable adsorption efficiency for the removal of Pb(II) and Cd(II) ions. Within 5 min, all the MgO samples adsorb around 99% of Pb(II) ions and 100% of Cd(II) ions. The adsorption of Pb(II) and Cd(II) ions increased with increase in adsorbate concentration, pH and temperature. The kinetics of Pb(II) and Cd(II) removal were fitted well to a pseudo-second-order model, and the Langmuir isotherm model better described their adsorption. By tuning morphology and surface textural properties of MgO in the presence of different anions, removal of other toxic metal ions from drinking water is of more significant from environmental point of view.

Acknowledgement

The authors would like to thank the Director of this Institute for his kind permission to publish this paper. The author, A.H.C is thankful to Jadavpur University for giving her permission to

carry out her M.Tech. Thesis work at CSIR-CGCRI, I.H.C is thankful to UGC for her fellowship and P.B is thankful to DST for fellowship. The work was funded by DST-SERB Project, Government of India (Grant No. SR/S3/ME/0035/2012) under the Project No. GAP 0616.

References

1. Q.L. Fang, S.H. Xuan, W.Q. Jiang and X.L. Gong, Adv. Funct. Mater. 2011, 21, 1902-1909.

2. D. Mohan and C. U. Pittman, J. Hazard. Mater., 2007, 142, 1-53.

3. Y. Jia, T. Luo, X-Y. Yu, B. Sun, J-H. Liu and X-J. Huang, RSC Advances 2013, 3, 5430-5437.

4. B.Q. Xu, J.M. Wei, H.Y. Wang, K.Q. Sun, Q.M. Zhu, Catal. Today 2001, 68, 217-225.

5. Y. Ding, G. Zhang, H. Wu, B. Hai, L. Wang, Y. Qian, Chem. Mater. 2001, 13, 435-440.

6. J.S. Mathews, O. Just, B. Obi-Johnson, W.S. Rees Jr., Chem. Vap. Deposition 2000, 6, 129-132.

7. J.J. Helble, J. Aerosol. Sci. 1998, 29, 721-736.

8. Q. Yang, J. Sha, L. Wang, Y.W. Wang, X.Y. Ma, J. Wang, D.R. Yang, Nanotechnology 2004,15, 1004-1008.

9. A.A. Al-Ghamdi, F. Al-Hazmi, F. Alnowaiser, R.M. Al-Tuwirqi, A.A. Al-Ghamdi, O.A. Alhartomy, F. El-Tantawy, F. Yakuphanoglu, J. Electroceram 2012, 29, 198-203.

10. W. Wang, X. Qiao, J. Chen, H. Li, Mater. Lett. 2007, 61, 3218-3220.

11. T. Selvamani, A. Sinhamahapatra, D. Bhattacharjya, I. Mukhopadhyay, Mater. Chem. Phys. 2011, 129, 853-861.

12. A.H. Chowdhury, I.H. Chowdhury, M.K. Naskar, Mater. Lett. 2015, 158, 190-193.

13. J. Roggenbuck, M. Tiemann, J. Am. Chem. Soc. 2005, 127, 1096-1097.

14. M. Bhagiyalakshmi, P. Hemalatha, M. Ganesh, P.M. Mei, H.T. Jang, Fuel 2011, 90, 1662-1667.

15. A. Tadjarodi, M. Sedghi, K. Bijanzard, J. Nanostructures 2012, 2, 273-278.

16. B. Nagappa, G.T. Chandrappa, Micropor. Mesopor Mater. 2007, 106, 212-218.

17. Y. Jia, X-Y. Yu, T. Luo, Z. Jin, B. Sun, J-H. Liu, X-J. Huang, Dalton Trans. 2014, 43, 2348-2351.

18. N. Khan, D. Dollimore, K. Alexander, F.W. Wilburn, Thermochimica Acta, 2001, 367-368, 321-333.

19. T. Lopez, I. Garcia-Cruz, R. Gomez, J. Catal. 1991, 127, 75-85.

20. L. Haurie, A.I. Fernandez, J.I. Velasco, J.M. Chimenos, J.M. Lopez-cuesta, F. Espiell, Mater. Res. Bull. 2007, 42, 1010-1018.

21. C.M. Janet, B. Viswanathan, R.P. Viswanath, T.K. Varadarajan, J. Phys. Chem C, 2007, 7, 10267-10272.

22. G. J. Boer, I.N. Sokolik and S. T. Martin, J. Quantitive Spectroscopy & Radiative Transfer, 2007, 108, 17-38.

23. L-Z. Pei, W-Y. Yin, J-F. Wang, J. Chen, C-G. Fan, Q-F. Zhang, Mater. Res., 2010, 13, 339-343.

24. C.M. Janet, B. Viswanathan, R. P. Viswanath and T. K. Varadarajan, J. Phys. Chem. C 2007, 111, 10267-10272.

25. M. Roy, S. Ghosh and M.K. Naskar, Dalton Trans., 2014, 43, 10248-10257.

26. N. Venkatachalam, P. Palanichamy and V. Murugesan, Mater. Chem. Phys., 2007, 104, 454-459.

27. H.G. Yang and H.C. Zeng, J. Phys. Chem B, 2004, 108, 3492-3495.

28. A. K. Bhattacharya, T. K. Naiya, S. N. Mandal and S. K. Das, Chem. Eng. J., 2008, 137, 529-541.

29. 1. J. Gong, T. Liu, X. Wang, X. Hu and L. Zhang, Environ. Sci. Technol., 2011, 45, 6181-6187.

30. C. Zhijiang, J. Jianru, Z. Qing and Y. Haizheng, *RSC Adv.*, 2015, 5, 82310-82323.

31. M. Shirani, A. Akbari and M. Hassani, *Anal. Methods*, 2015, 7, 6012-6020.

32. C-Y. Cao, J. Qu, F. Wei, H. Liu and W-G. Song, ACS Appl. Mater. & Interface, 2012, 4 4283-4287.

33. Y. Zhuang, Y. Yang, G. Xiang, and X. Wang, J. Phys. Chem. C, 2009, 113, 10441-10445.

34. Y. Wang, G. Wang, H. Wang, C. Liang, W. Cai, and L. Zang, J. Eurp. Chem, 2010, 16, 3497-3503.

35. K. G. Sreejalekshmi, K. A. Krishnan and T.S. Anirudhan, J Hazard Mater, 2009, 161,1506–1513.

36. M. Iqbal and R. Edyvean, Miner. Eng, 2004, 17, 217–223.

37. X. Yang, X. Wang, Y. Feng, G. Zhang, T. Wang, W. Song, C. Shu, L. Jiang. and C. Wang, J. Mater. Chem. A, 2013, 1, 473-477.

38. M. Arshadi, M.J. Amiri and S. Mousavi, Water Resources and Industry, 2014 6, 1–17.

Graphical Representation

MgO nanostructures with controllable morphology and tunable textural properties synthesized via aqueous based route in the absence of organic templates were found to be excellent adsorbent for the removal of Pb(II) and Cd(II) ions from water